

# Nanoscale

Accepted Manuscript



This is an *Accepted Manuscript*, which has been through the RSC Publishing peer review process and has been accepted for publication.

*Accepted Manuscripts* are published online shortly after acceptance, which is prior to technical editing, formatting and proof reading. This free service from RSC Publishing allows authors to make their results available to the community, in citable form, before publication of the edited article. This *Accepted Manuscript* will be replaced by the edited and formatted *Advance Article* as soon as this is available.

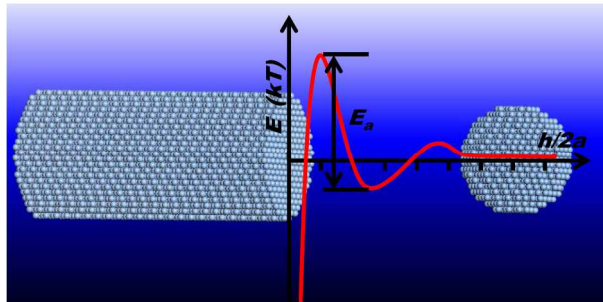
To cite this manuscript please use its permanent Digital Object Identifier (DOI®), which is identical for all formats of publication.

More information about *Accepted Manuscripts* can be found in the [Information for Authors](#).

Please note that technical editing may introduce minor changes to the text and/or graphics contained in the manuscript submitted by the author(s) which may alter content, and that the standard [Terms & Conditions](#) and the [ethical guidelines](#) that apply to the journal are still applicable. In no event shall the RSC be held responsible for any errors or omissions in these *Accepted Manuscript* manuscripts or any consequences arising from the use of any information contained in them.

**Table of content:**

Experimental and theoretical findings on the energies associated with the oriented-attachment nanocrystal growth are reviewed systematically in this article.

**Graphical abstract:**

## Understanding the oriented-attachment growth of nanocrystals from an energy point of view: A review

Weiqliang Lv<sup>1,2</sup>, Weidong He<sup>1,3,4\*</sup>, Xiaoning Wang<sup>1</sup>, Yinghua Niu<sup>5</sup>, Huanqi Cao<sup>1</sup>, James H. Dickerson<sup>6,7</sup>,

Zhiguo Wang<sup>8</sup>

<sup>1</sup> School of Energy Science and Engineering, University of Electronic Science and Technology of China (UESTC), Chengdu 611731, PR China, <sup>2</sup> Department of Chemistry, the Hong Kong University of Science and Technology, Clear Water Bay, Hong Kong SAR, <sup>3</sup> Interdisciplinary Program in Materials Science, Vanderbilt University, Nashville, Tennessee 37234-0106, USA, <sup>4</sup> Vanderbilt Institute of Nanoscale Science and Engineering, Vanderbilt University, Nashville, Tennessee 37234-0106, USA, <sup>5</sup> School of Chemical Engineering, Harbin Institute of Technology, Harbin 150001, China, <sup>6</sup> Center for Functional Nanomaterials, Brookhaven National Laboratory, Upton, NY 11973, US, <sup>7</sup> Department of Physics, Brown University, Providence, RI 02912, US <sup>8</sup> Department of Applied Physics, University of Electronic Science and Technology of China, Chengdu, 610054, PR China. Correspondence and requests for materials should be addressed to W. H. (Email: weidong.he@uestc.edu.cn, weidong.he@vanderbilt.edu).

### Abstract

Since Penn *et al.* first discovered the oriented attachment growth of crystals, the oriented attachment mechanism has now become the major research focus in the crystal field and extensive efforts have been carried out in the past decade to systematically investigate the growth mechanism and the statistical kinetic models. However, most of the work mainly focuses on the experimental results in the oriented attachment growth. Different from the previous reviews, our review overviews the recent theoretical advances in the oriented attachment kinetics combined with experimental evidences. After a brief introduction to the van der Waals interaction and Coulombic interaction in a colloidal system, the correlation between the kinetic models of the oriented attachment growth and the interactions is then our focus. The impact of *in-situ* experimental observation techniques on the study of oriented attachment growth is examined with insightful examples. In addition, the advances in theoretical simulations mainly investigating the thermodynamic origin of these interactions at the atomic level are reviewed. The review seeks to understand the

oriented attachment crystal growth from a kinetic point of view and provide quantitative methodology to rationally design an oriented attachment system with pre-evaluated crystal growth parameters.

## 1. Introduction

The oriented attachment (OA) is a typical ‘match and dock’ growth mechanism of nanocrystals (NCs).<sup>1</sup> In recent years, the OA growth has shown great potential in controlling and designing materials of various nanostructures including zero-dimensional (0D) nanoparticles (NPs), one dimensional (1D) nanorods (NRs) /nanowires (NWs), two dimensional (2D) nanosheets (NSs) and macroscopic objects. The typical examples reported since 2010 are given in Table 1. In addition, several insightful reviews have also been published recently in this area.<sup>2-5</sup> For examples reported before 2010, one can refer to ref. [4-5]. Efforts are not only centered on the development of novel OA structures of various materials and their functional properties, but are also centered on the comprehensive insight of the mechanism and kinetics; the efforts seek to understand the fundamental scientific basis associated with the dynamic OA growth. Many efforts have been executed to develop OA kinetic models from a statistical point of view. Typical strategies include fitting the size evolution of NPs as the OA growth proceeds, treating NPs as ‘molecules’ and assuming the OA growth is driven via collision and reaction of molecules. These models range from simple dimer formation models, which are mathematically simple and easy to manipulate, to data sets tracking primarily on particle concentration, to polymerization models describing the number of primary particles per secondary

particle, to population balance models employing Derjaguin-Landau-Verwey-Overbeek (DLVO) theory which predicts the size distribution of secondary particles, and then to the effects of suspension conditions on the kinetics of oriented aggregation. However, these statistical models cannot explain what the driving force of the OA is, how NPs attach to each other or why the resulted shapes of materials are formed. To answer these fundamental questions, one must take a different approach to understand the ordered assembly of OA NPs. The 0D, 1D, 2D, 3D morphologies achieved via OA can be described by non-covalent interactions between different assembly objects (NPs, NRs or other complex aggregations), including the van der Waals interactions (vdW), Coulombic interaction (CI), and dipolar interaction (DI). These interactions, which are typically in the range of 0–10  $k_B T$ , are much weaker than the interaction of covalent bonds (ca. 100–150  $k_B T$ ). OA growth kinetics can be built via the study of these interactions. The recently-derived analytical expressions of vdW and CI allow one to evaluate the correlation between the kinetics of OA NRs and the important growth parameters including the NP-NR separation, the diameter of NPs and the aspect ratio (AR) of the growing NR. In this review, the interactions between colloidal NCs based on the classical DLVO theory are first introduced. Due to the drawback of analyzing the dynamic growth process of anisotropic OA NCs via the DLVO, an improved model for OA NRs is then highlighted. The overview on the simulations at the atomic level follows that focuses on the origin of these interactions and building the connection of the interactions with various materials and crystal structures. In the end, *in-situ* experimental observation techniques which provide

direct evidence for the interactions and their roles in the assembly of OA NPs, are discussed. In short, the review looks into the thermodynamic origin of the OA growth by over-viewing the recent study of the OA growth kinetics. The review seeks to improve our understanding of the OA crystal growth mechanism and facilitate the design of the growth of OA nanomaterials with desirable morphologies and properties.

**Table 1.** Examples of OA nanocrystals reported since 2010.

Year	First Author	Matter	Morphology	Ref.
2010	Almeida	$\alpha$ -Fe <sub>2</sub> O <sub>3</sub>	nanorods	6
2010	Choi	SrMoO <sub>4</sub>	wires, notched spheres	7
2010	Christy	TiO <sub>2</sub>	nanorods	8
2010	Cui	NaTAO <sub>3</sub>	porous microsphere	9
2010	Gunning	CdS	nanorods	10
2010	Kim	$\beta$ -In <sub>2</sub> S <sub>3</sub>	nanotubes	11
2010	Koh	PbSe	nanorods	12
2010	Lo	FeP <sub>3</sub>	nanorods	13
2010	Ning	SnTe	nanoparticles and nanowires	14
2010	Schliehe	PbS	ultrathin sheets	15
2010	Srivastava	CdS	nanowires	16
2010	Zheng	CdS	quantum dots	17
2011	Chang	CuInSe <sub>2</sub>	nanoflowers, nanowires branched multipods	18
2011	Chen	$\alpha$ -Fe <sub>2</sub> O <sub>3</sub>	1D chain-like structures 2D layers 3D superstructure	19
2011	Da Silva	anatase TiO <sub>2</sub>	mesocrystals with Wulff shape	20
2011	Dong	(BiO) <sub>2</sub> CO <sub>3</sub>	hierarchical hollow microspheres	21, 22
2011	Duan	CdSe	dendrites	23
2011	Fei	BiFeO <sub>3</sub>	pills and rods	24
2011	He	EuS	nanoclusters, nanorods	25
2011	Huang	ZnO	nanorods	26
2011	Jin	PbS	nanorods	27
2011	Koziej	MoO <sub>2</sub>	nanorods	28
2011	Krishnadas	Ni	nanowires	29
2011	Li	V <sub>2</sub> O <sub>5</sub>	ultra-long nanobelts	30
2011	Li	CdS	nanorods	31
2011	Lin	BN	hexagonal nanocrystals	32
2011	Liu	ZnO	3D mesoporous ellipsoids	33
2011	Moreira	BaZrO <sub>3</sub>	3D deca-octahedral architecture	34
2011	Sliem	PbSe	nanocubes	35
2011	Stroppa	SnO <sub>2</sub>	nanoparticles with elongated shape	36
2011	Taniguchi	CeO <sub>2</sub>	nanocubes	37
2011	Tian	GdF <sub>3</sub>	nanowires	38
2011	Vaughn	SnSe	nanosheets	39
2011	Wang	Bi <sub>2</sub> Te <sub>3</sub>	nanowires	40,41
2011	Wang	Cu <sub>7</sub> Te <sub>4</sub>	sheet-like particles	42
2011	Wang	Sb <sub>2</sub> O <sub>3</sub>	nanorod-bundles	43
2011	Yella	WO <sub>3</sub>	asymmetric nanobrushes	44
2011	Yin	BaWO <sub>4</sub>	shuttle-like, ellipsoid-like, and flower-like structures	45
2011	Zhang	Bi <sub>2</sub> S <sub>3</sub>	nanorods and nanosheets	46
2012	Burrows	$\alpha$ -FeOOH	acicular nanorods	47
2012	Chen	WO <sub>3</sub>	ultrathin, nanosheets	48
2012	Distaso	ZnO	twin nanorods	49
2012	Dong	BiOI/BiOCl	nanoplates microflowers	50
2012	Douglas	lanthanide oxide (CeO <sub>2</sub> , Nd <sub>2</sub> O <sub>3</sub> , Eu <sub>2</sub> O <sub>3</sub> , Gd <sub>2</sub> O <sub>3</sub> , Dy <sub>2</sub> O <sub>3</sub> , Yb <sub>2</sub> O <sub>3</sub> )	nanoribbons ultra-thin nanowires	51
2012	Ji	$\beta$ -MnO <sub>2</sub>	hollow polyhedral nanorods	52
2012	Kim	PbSe	nanorods	53
2012	Li	Cd(OH) <sub>2</sub>	pancake-like superstructures	54

2012	Liang	Ag	nanorices	55
2012	Liu	ZnO	twin-brush mesocrystals	56
2012	Liu	Ag	nanoplates	57
2012	Ludi	ZnO	nanorods, fan- or bouquet-like bundles	58
2012	Wang	SnO <sub>2</sub>	ultrathin nanosheets	59
2012	Wang	rutile TiO <sub>2</sub>	branched nanorods hierarchical mesocrystals	60
2013	Cao	ZnO	hierarchical leaf- and flower-like structures.	61
2013	Cui	BiOCl	nanosheets	62
2013	Li	Sb <sub>2</sub> O <sub>3</sub>	nanobelt bundles	63
2013	Li	TiO <sub>2</sub>	highly branched nanowires	64
2013	Li	anatase TiO <sub>2</sub>	nanosheet array	65
2013	Li	WO <sub>3</sub>	nanotube-based bundles	66
2013	Liu	CaCO <sub>3</sub> ·H <sub>2</sub> O	dumbbell-like superstructures	67
2013	Nootchanat	Au	nanosheets	68
2013	Shuai	α-Zr <sub>3</sub> (PO <sub>4</sub> ) <sub>4</sub>	layered nanodisks	69
2013	Song	SnO <sub>2</sub>	nanorods	70
2013	Yu	Pt-M (M = Cu, Co, Ni, Fe)	worm-like nanowires	71

## 2. OA growth kinetics

### 2.1 Roles of vdW and CI interactions in a colloidal system-the DLVO theory

The DLVO theory assumes that the interaction potential energy ( $E_{DLVO}$ ) for two spherical particles of the same size separated by a distance  $h$  (the shortest distance between two spherical particles, each having a radius of  $a$  and a center-to-center distance of  $r$ , and  $h = r - 2a$ ) is the sum of the repulsive electrostatic energy of the electric double layers ( $E_{EDL}$ ) and the attractive vdW energy ( $E_{vdW}$ ) of attraction between adjacent particles, which is given in Eq. 1.

$$E_{DLVO} = E_{vdW} + E_{EDL} \quad (1)$$

The derivation of  $E_{EDL}$  and  $E_{vdW}$  between two colloidal NPs can be found in the literature.<sup>72-74</sup> The interaction potential for two colloidal NPs versus their separation can be plotted, as shown in Figure 1. The energy barrier or the activation energy ( $E_a$ ) of the ‘attachment’ reaction between two particles can be obtained based on the difference between the maximum and the minimum of  $E_{DLVO}$  which is a function of inter-particle separation. With the calculated values of these interactions and  $E_a$ , the kinetic constant of the OA growth can be directly determined via the famous

Arrhenius equation, as given in Eq. 2.

$$k = Ae^{-E_a/RT} \quad (2)$$

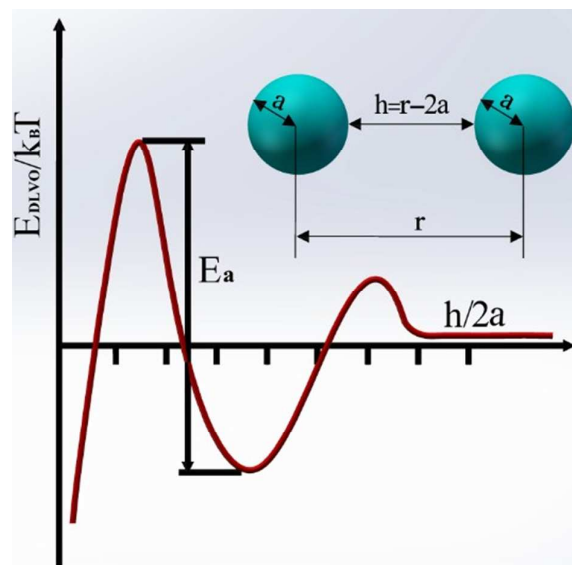


**Figure 1.** Interaction potential versus separation between two spherical colloidal NPs.

The DLVO theory accounts for the effects of ionic strength, pH, surface potential, Hamaker coefficient and dielectric constant. However, additional forces besides the DLVO construction, such as H-bonding, steric force and hydration force, have also been reported to affect the colloid stability.<sup>75</sup> DLVO is not effective in describing the correlation between the formation of colloidal crystals and the atomic structure of the crystal surface.<sup>76</sup> Further, the dynamic size change of OA crystals with non-spherical shapes cannot be investigated by the DLVO model.

## 2.2 A model for growing OA NR: roles of vdW and CI

To develop a model that works with anisotropic OA crystals can provide more insightful information about the OA mechanism. To study the OA mechanism, a portion of such work has been done by constructing analytical models.<sup>77</sup> The theoretical construction of 1D OA nanostructures largely facilitates the understanding

of the kinetic process of the OA growth. It was assumed that spherical NPs are attached to the two sides of a cylindrical NR and then grow into 1D OA NCs. The primary monomers (NPs that are used as precursors at the initial stage) are assumed to be spherical NPs with a radius of  $R_2$ . The growing NR is assumed to be cylindrical with a continuously increasing AR. In the OA growth, spherical NPs driven by the inter-particle interactions typically attach to one end of the growing 1D NRs. The growth model is demonstrated in Figure 2. With the incorporation of AR, the NP-NR model allows for the evaluation of the NP-NR interactions during the entire dynamic growth of the OA NRs. Since the activation energy of the OA growth is primarily a function of CI, vdW and DI, the analytical expressions of these interactions are necessary to evaluate the correlation between their dynamic evolutions with the important parameters associated with the OA growth. The evaluation of the interactions enables one to design efficient parameters for the OA growth before the actual synthesis of the OA NCs, including the NP size, the aspect ratio of a growing NR or nanotube (NT), the concentration of the precursor NPs, the surfactants and the solvents.

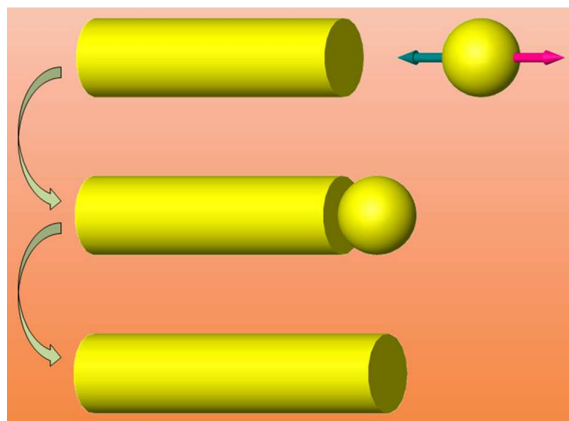


**Figure 2.** Demonstration of the NR growth via the oriented attachment of one monomer NP to one end of the NR. Reproduced from ref. [77] with permission from *The Royal Society of Chemistry*.

### 2.2.1 vdW interaction

The analytical expression of the vdW interaction between an attaching NP and a growing 1D nanostructure was derived.<sup>78</sup> In the derivation, aspect ratio was introduced to evaluate the vdW during the entire dynamic growth of OA NRs.<sup>78</sup> The derivation was based on the Hamaker's particle–particle model and was adopted as the platform to explore the role of the vdW interaction in the formation of 1D OA NRs from NP precursors. The vdW interaction between two spherical particles is given by Eq. 3,

$$E = - \int dv_1 \int dv_2 \frac{q^2 \lambda}{r^6} \quad (3)$$

where  $v_1$  and  $v_2$  are the respective volumes of the two particles,  $r$  is the distance between the two particles,  $q$  is the atomic concentration of the particles, and  $\lambda$  is the vdW constant. A two-step integration approach was adopted in the derivation. First, the vdW between the entire cylinder and a single point within the sphere was calculated. Second, this solution was used as the basis to integrate over the entire sphere, yielding the vdW between the two objects. Through the vdW expression, the

correlation between vdW and the important growth parameters including the dimension and separation of NP and NR, the Hamaker constant and the attachment orientation, was evaluated, as shown in Figure 3. To evaluate the critical separation at which the vdW interaction between the NP and the NR is negligible, the critical center-center separation ( $C_c$ , indicated by the vertical dotted line in Figure 3A) and critical surface-to-surface separation ( $D$ ,  $D = C_c - L/2 - R_2$ ,  $L$  is the length of the NR,  $R_2$  is radius of NP) were proposed. The value of vdW smaller than  $-0.5\% k_B T$  was negligible, as marked by the horizontal dotted line in Figure 3. The dramatically rapid drop in vdW with increasing  $C$  verifies that the vdW interaction is a short-range force (Figure 3A). The critical separation ( $D$ ) increases nearly linearly with the radius of NPs ( $R_2$ ) as shown in the inset of Figure 3A, which implies that if the vdW dominates the growth, NRs with a larger size will grow faster when the effect of Brownian motion is neglected.  $D$  is nearly constant as  $AR$  varies (Figure 3B), which suggests that the growth rate remains constant as the growth of  $AR$  via OA proceeds. However, the change of other factors, such as the dramatic decrease of the diffusion and Brownian motion as the size and mass of NRs increase, slows down the OA growth process.  $D$  increases asymptotically with the Hamaker constant ( $A$ ), indicating the limited influence of  $A$  (Figure 3C). This may explain why a change of the surfactant and an increase of the synthetic temperature cannot increase the growth rate while the increase in the concentration and size of the primary NP monomer precursors increases the growth kinetics. The weaker vdW interaction in the off-axis approach of NPs to the growing NR suggests that the head to head attachment is favored during

the growth of 1D OA NRs (Figure 3D). Such theoretical investigation into the growth of NRs provides the basis for comprehending the role of vdW, and the guidance for the efficient synthesis of 1D nanostructures.

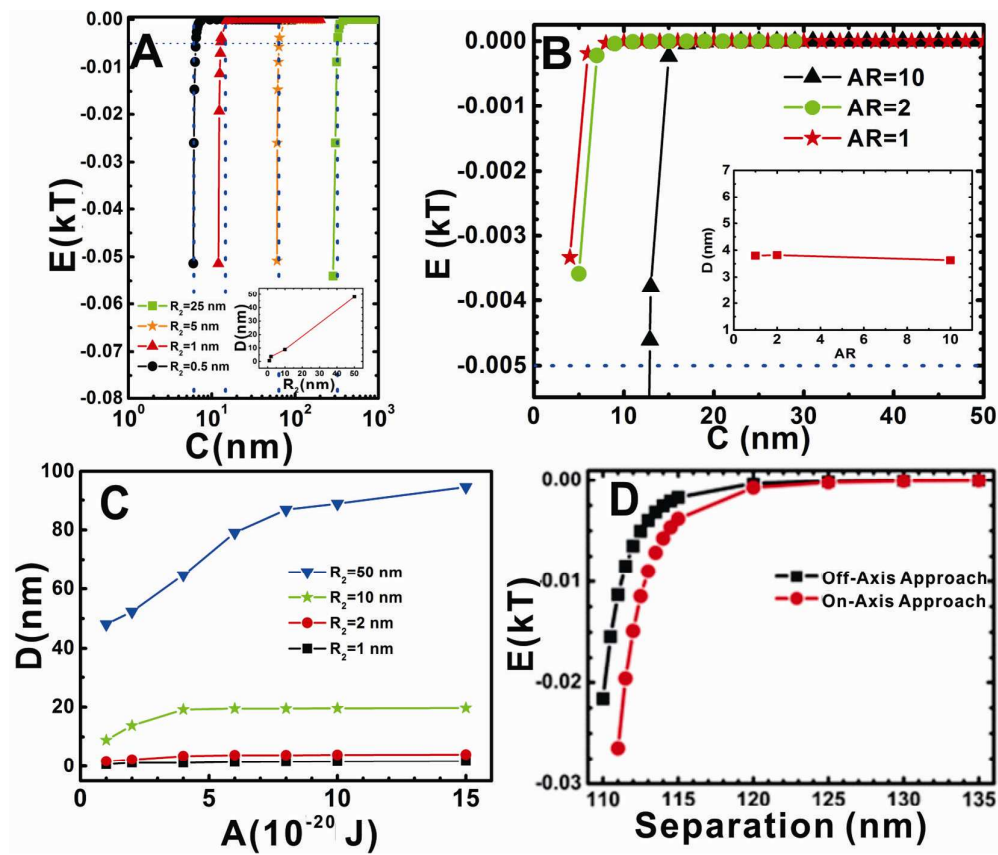


**Figure 3.** The correlations between vdW and the parameters associated with the dimension and separation of NP and NR. (A) Graphs of vdW versus  $C$  for NRs with different diameters. Insert: plot of  $D$  versus  $R_2$ ; (B) Graphs of vdW versus  $C$  for NRs with different ARs and of a fixed diameter of 2 nm; (C) Graphs of  $D$  versus  $A$  with different  $R_2$  and a fixed AR of 10; (D) Graphs of the vdW interaction versus the separation between a NP (diameter: 10 nm) and a NR (diameter: 10 nm and AR: 20). Reproduced from ref. [78] with permission from the *PCCP Owner Societies*.

### 2.2.2 Coulombic interaction

In a colloidal system, strongly-charged surface surfactants hinder the Ostwald ripening (OR) growth at the initial stage to promote the OA growth, and thus they are frequently employed to facilitate the successful synthesis of various well-defined 1D, 2D and 3D materials with ‘focused’ size distributions and desired structures. The

adsorption of charged surface adsorbents and ions on NP monomers creates strong coulombic interactions between the NPs, and largely affects the kinetics of the OA process. To illustrate the role of CI in an OA growth, the accurate calculation of CI is desirable. The analytical expression of CI was derived via the same NR-NP model and based on the expression of the CI between two point charges,<sup>77</sup> as described by the Coulomb's law in Eq. 4,

$$E = \frac{1}{4\pi\epsilon} \frac{Q_1 Q_2}{r} \quad (4)$$

where  $Q_1$  and  $Q_2$  are the charge values of point 1 and point 2,  $r$  is the separation between point 1 and point 2, and  $\epsilon$  is the dielectric constant of the medium. The above equation was then employed as the integration unit to obtain the analytical expression of CI between a spherical NP and a cylindrical NR with the incorporation of the important parameters in the OA growth, including the NP size, the AR of the growing NR and the NP-NR separation, as shown in Eq. 5,

$$E_{CI} = \frac{1}{4\pi\epsilon} 8\pi^2 \sigma^2 r_1^2 \left[ r_2 \left( \ln \frac{a+c+\frac{l}{2}}{b+c-\frac{l}{2}} \right) + (a+c-2c) \right] \quad (5)$$

where  $\sigma$  is the surface charge density of the NP and the NR,  $r$  is the radius of the NP and the NR,  $l$  is the length of the NR,  $c$  is the NP-NR separation,  $\epsilon$  is the dielectric constant of the medium and

$$a = \sqrt{\left(c + \frac{l}{2}\right)^2 + r_2^2}, \quad b = \sqrt{\left(c - \frac{l}{2}\right)^2 + r_2^2}$$

The surface charge density and the dielectric constant are related to the nature of the materials to be synthesized, the concentration of the NP precursor, the surfactant used to control the growth direction, and the nature of the solvents. The increase of AR

describes the dynamic growth process of the NR, this simple analytical form of CI provides an efficient platform for the evaluation of CI in a variety of OA growth systems. For instance, the long-range feature of the CI interaction (see Figure 3A and Figure 4) indicates that a medium with a higher precursor concentration and with a higher temperature is favorable to obtain small particle separation and facilitates the fast growth of OA NRs. The evaluation of CI versus AR shows that CI gets saturated when AR reaches a certain value, which indicates that the OA growth is inhibited when the NRs grow to a certain large length. This statement is confirmed by the long-existing challenge of synthesizing OA NRs or NWs with high ARs in experiments.

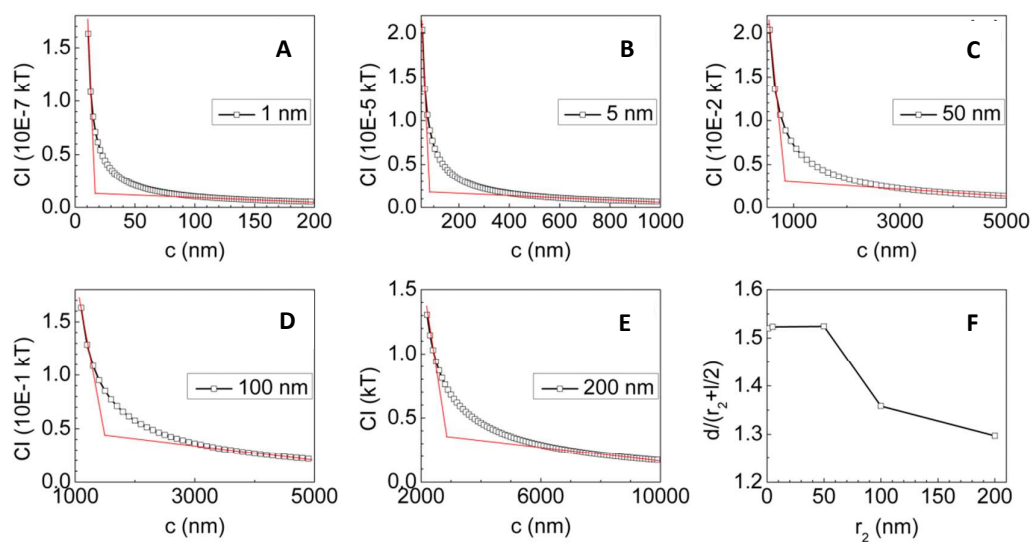


**Figure 4.** (A–E) Graphics of CI versus  $c$  for NRs of different radii. For each graph, the critical point  $d$  is the  $c$  value of the crossing point of the two red lines. All graphs assume  $AR = 10$ ,  $T = 300$  K, dielectric constant = 80 (water solvent), and charge density =  $30\,000/\pi$  electrons  $\text{nm}^{-2}$ , and (F) the plot of  $d/(r_2 + l/2)$  versus  $r_2$ . Reproduced from ref. [77] with permission from *The Royal Society of Chemistry*.

Figure 5A shows that CI decreases gradually as the temperature increases, which suggests that increasing the temperature can reduce the energy barrier of an OA growth.<sup>79</sup> The decrease of CI with the increase of temperature is abrupt for NRs with large ARs, indicating that the formation of long OA NRs at high temperatures is more

thermodynamically favorable compared to short NRs. This finding is consistent with our previous experimental observation of the long EuS NRs at high temperatures.<sup>25</sup> The increase of CI with increasing surface charge density of NRs and the more abrupt such trend for long OA NRs, as shown in Figure 5B, suggest too large a charge density is detrimental to the growth of long/ultra-long OA NRs. Suitable ligands should be employed to control the charge density at a proper level while maintaining sufficient stability in the OA growth of long NRs.

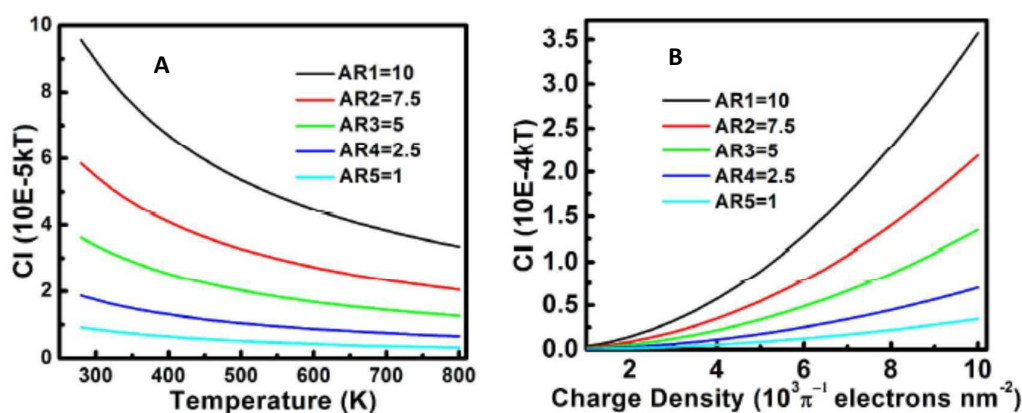


**Figure 5.** Plots of the CI interaction *versus* (A) temperature and (B) charge density for NRs of different ARs. For all the plots,  $c = 60$  nm, dielectric constant = 80 (water solvent), and in plot (A), charge density =  $(50000/\pi)$  electrons/nm<sup>2</sup>. Reproduced from ref. [79] with permission from *The Royal Society of Chemistry*.

Due to the high efficiency of the model and the analytical interaction expressions for evaluating the growth of OA NRs, this model was employed to evaluate the growth of OA nanotubes,<sup>80</sup> which was recently observed in experiment.<sup>81</sup> A 3D demonstration of two NPs attaching to the two ends of a growing NT is shown in Figure 6. The derivation of the CI expression is similar to the derivation of the expression between a NP and a NR. The detailed expression of CI between a NP and a NT can be found in ref. [80].  $r_0$  is the radius of the NP, and  $r_1$  and  $r_2$  represent the radii of outer and inner radii of the NT,  $c$  is the separation between the NT and the NP, and

$l$  represents the length of the NT.

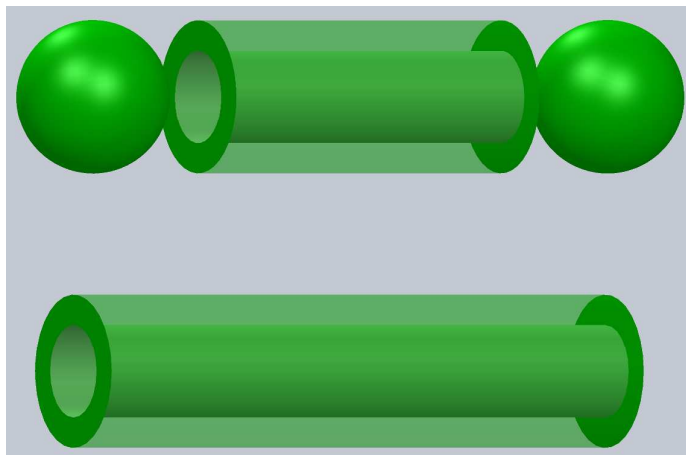


**Figure 6.** A 3D model of two NPs attaching to two ends of a growing NT. Reproduced from ref. [80] with permission from *The Royal Society of Chemistry*.

CI increases rapidly as the NP-NT separation decreases and there exists an inflexion point  $d$  where the increasing rate begins to increase abruptly. This indicates that too large a precursor concentration is detrimental to the OA growth of NTs. The CI increases with increasing outer NT radius (Figure 7A) and this suggests that large NTs experience larger growth energy barriers compared with small NTs. A dilute precursor solution may favor the synthesis of OA NTs with relatively large radii. Figure 7B shows that CI increases with the increase of AR, suggesting that the elongation of NTs experiences higher CI energy barriers as their length increases, which is consistent with the earlier theoretical report on the growth of NRs.<sup>77</sup>

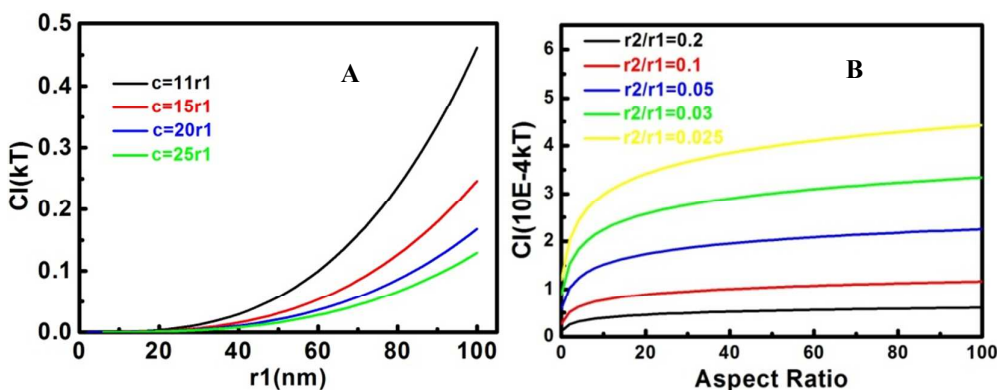


**Figure 7.** (A) Plots of CI versus  $r_1$  for NTs of different NP-NT separations, assuming  $AR = 10$ ,  $r_2/r_1 = 0.5$ ,  $l = 20 r_1$ ,  $r_0 = r_1$ ,  $T = 300$  K, dielectric constant of water solvent=80, and charge density= $30000/\pi$  electrons/nm<sup>2</sup>. (B) Plots of the CI versus AR, assuming the NT and the NP are attaching,  $r_0 = r_2 = 2.5$  nm, and  $l = ARr_1 + r_0$ . Reproduced from ref. [80] with permission from *The Royal Society of Chemistry*.

### 2.3 Theoretical simulations of OA process: origin from crystals structures

Improving the capability of designing a growth system of OA crystals is a promising research direction since it allows for the synthesis of materials with novel structures, well-defined shapes and sizes. The investigation into the thermodynamic origin on the atomic scale can largely improve our understanding on the kinetics of the OA growth. The molecular dynamics (MD), Monte Carlo (MC) and density functional theory (DFT) can simulate the NP aggregation and reveal the details of the OA process, which are not accessible in experiments.

Molecular calculations demonstrate the importance of CI in controlling the OA growth. Through molecular energetic calculations, Zhang *et al.* studied the role of vdW and CI interactions to the lattice orientations of the resulted OA crystals.<sup>82</sup> Assuming that the NPs are initially separated by an infinite distance, they simulated the energy change in the OA ( $\Delta E_{OA}$ ) attachment of two 4 nm spherical NPs on different ( $hkl$ ) surfaces, as shown in Figure 8. It is found that the thermodynamic driving force for the OA attachment arises from both the interatomic interactions in

the attaching NPs and the surface energy of the attaching surfaces. Based on the OA energy as a function of crystallographic orientation, they also predicted the favored OA growth orientations, and the predictions are consistent with experimental observations. The CI interaction, stemmed primarily from the crystal structures, makes much more contributions to  $\Delta E_{OA}$  compared to the vdW interaction. The molecular energetic calculation based on the interatomic potentials including CI and vdW, provides the basis for understanding why sequential attachment events generate crystals with morphologies not predicted from the symmetry of the material. The computational prediction of initial and sequential OA attachment events facilitates the experimental studies and improves the efficiency of materials design efforts.

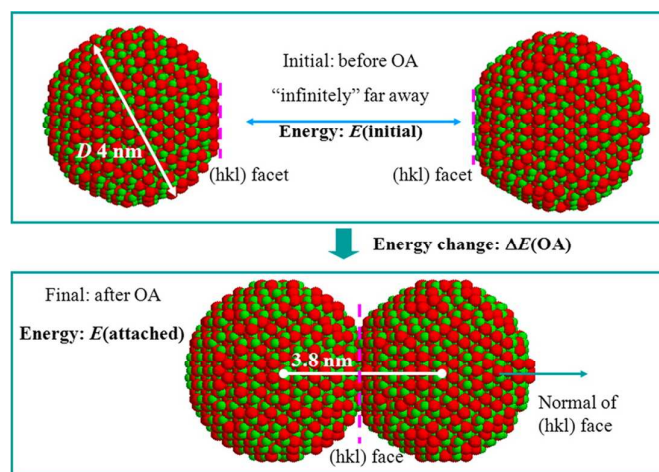


**Figure 8.** Diagram showing an OA process in which two 4 nm particles are attached on an  $(hkl)$  surface. Reproduced with permission from ref. [82]. Copyright (2012) *American Chemical Society*.

Molecular dynamic simulation was employed to study the electrostatic forces between under-coordinated atoms on the surface of NPs and reveal the preferred alignment of OA NPs. Alimohammadi *et al.* employed classical MD simulation to study the aggregation of  $\text{TiO}_2$  NPs with both Wulff shapes and asymmetric shapes.<sup>83</sup>

Figure 9 shows the MD aggregation process for symmetric NPs. The two NPs are first

separated by a distance of  $\sim 8.5$  nm (Figure 9A), and then the two NPs begin to rotate and approach to each other in the Matsui-Akaogi force field which includes the vdW term and CI term. The two NPs first rotate in the attaching orientation upon aggregation (Figure 9B). Then the (001) surface of one NP contacts the edge between two (101) facets of the other NP to form a ‘hinge’ pattern through the chemical bonding between under-coordinated Ti and O atoms (Figure 9C). At the end, the two NPs rotate around the hinge such that the (101) facet of one NP contacts the (001) facet of the other NP (Figure 9D). The total CI interaction is consistently ten times larger than the sum of the vdW and other interactions, indicating the dominant impact of CI on the alignment of OA NPs. They further clarified that the CI interaction arises from the under-coordinated atoms on the surface and edge of the NPs. Since a symmetric NP with a Wulff shape shows no ex-dipole moment, they ascribed the directional attachment to the high-order multi-poles which are created by positive and negative charges associated with under-coordinated surface atoms.

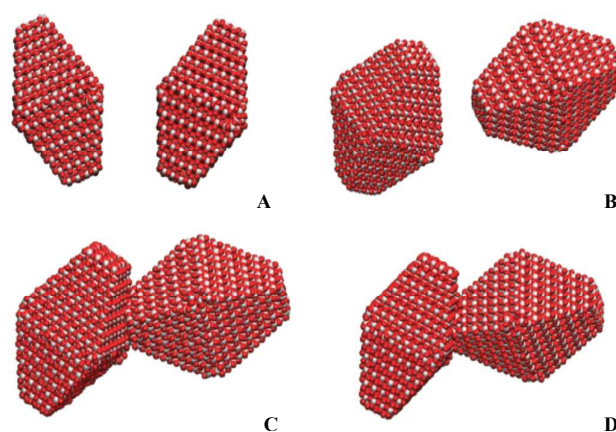


**Figure 9.** Snapshots of the aggregation of the large symmetric NCs in MD simulation. These figures are taken (A) at the beginning of the simulation; (B) after 100 ps; (C) after 160 ps; and (D) after 1.0 ns. Oxygen atoms are shown in red (dark) and titanium atoms are shown in white (light). Reproduced with permission from ref. [83]. Copyright (2009) *American Chemical Society*.

Chemical environments such as solvent can largely influence the interaction between NPs and thus influence the OA growth. Sathiyarayanan *et al.* found that solvent plays an important role in promoting the anisotropic growth of colloidal nanostructures.<sup>84</sup> They proposed that two NCs approach each other and form a mesocrystal configuration at a minimum free energy state, in which the two particles hover next to each other with facets in parallel and separated with one or two layers of solvent molecules. MD simulations in Figure 10 show that solvent ordering is disrupted at the edges of NCs where initial contact between two nanoparticles is most likely to occur. The free-energy barriers for NC aggregation are smallest on the smallest facets where the smaller nanoparticle is in close proximity to the edge of the larger one.<sup>84</sup> This simulation demonstrates that even without surfactant or ligand, anisotropic growth is still possible with certain solvents. Similar experimental phenomenon was also observed by Giersig *et al.*<sup>85</sup>

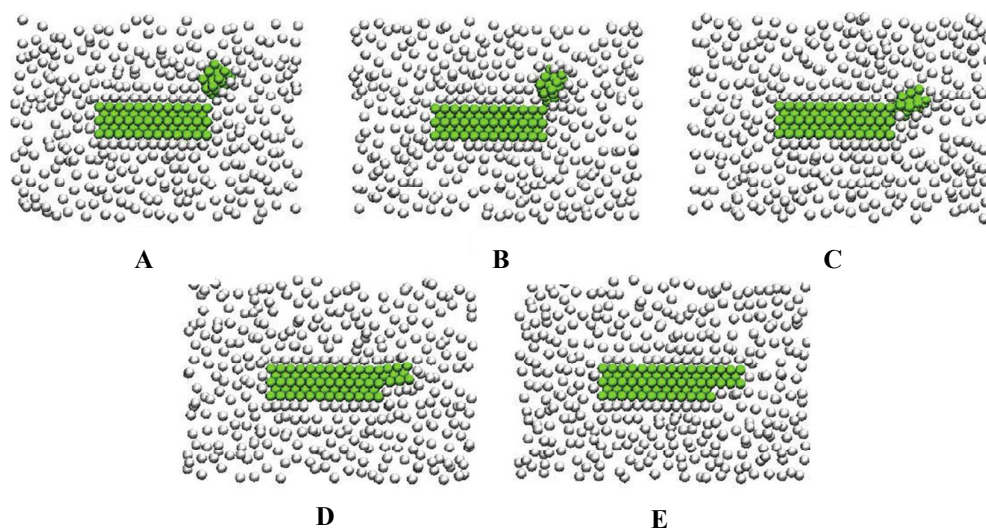


**Figure 10.** MD time sequence of nanoparticle configurations when a small nanocrystal approaches the edge of the nanoplate. (A) The initial nanoparticle configuration. (B) First contact of the two NCs. (C-D) Alignment of the two NCs. The smaller one undergoes rotation. (E) Final formation of a monocrystal. Reproduced with permission from ref. [84]. Copyright (2011) *American Chemical Society*.

Fusion between NPs is another phenomenon that might be related to the aforementioned three types of interactions between NPs. Schapotschnikow *et al.*

found that two uncapped nanocrystals can fuse via direct surface attachment when they are placed close, regardless of their initial configuration, as shown in Figure 11.<sup>86</sup> The fusion between two misaligned NCs can be divided into two stages. First, the two NCs adjust their orientations to bring their edges into contact. Second, the two NCs continue to adjust their orientations to close the gap. They also stated that the interparticle dipolar interaction plays an insignificant role in OA growth. DI will be discussed in detail in a later section.

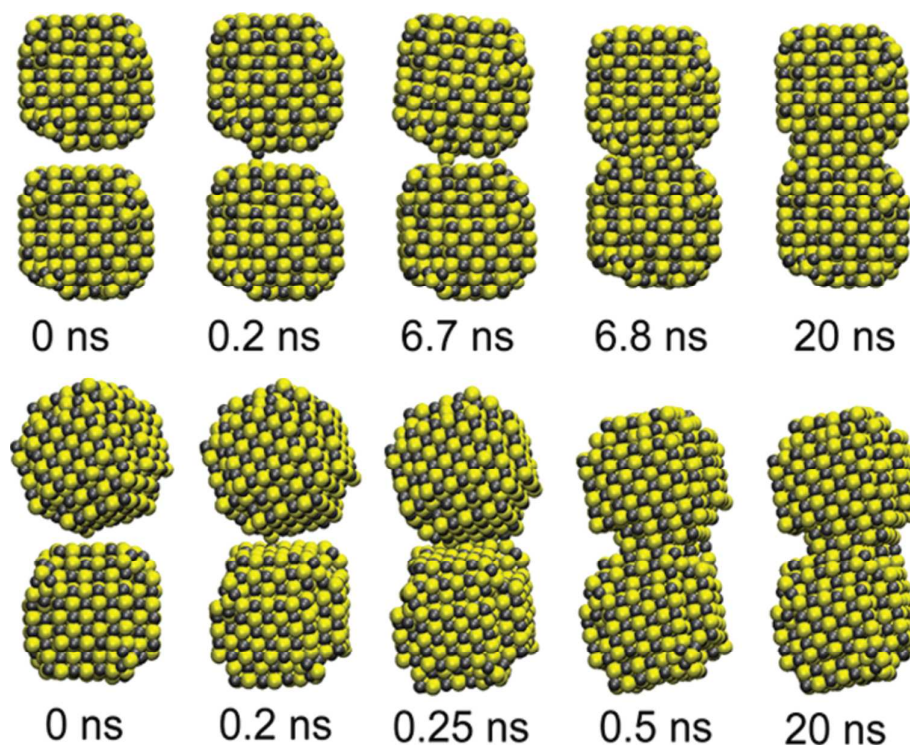


**Figure 11.** Fusion of two PbSe NCs. Top: The NCs are initially  $\{100\}$  facet-to-facet aligned. Bottom: The NCs have an initial mistilt in two directions of  $27^\circ$  and  $11^\circ$ , respectively. Reproduced with permission from ref. [86]. Copyright (2010) *American Chemical Society*.

The MD simulations and DFT calculations are frequently employed to probe the OA growth at the atomic scale. vdW, CI, DI and other interactions between NCs of arbitrary shapes and with arbitrary distances can be quantitatively evaluated through

MD and DFT. Insightful results can be obtained by building rational models. Nonetheless, one should always keep in mind that many computations actually ignore some important variables including those from the chemical environments around NCs, such as ligands, surfactants, solvent molecules and ions on the surface of NCs. The ligands not only possibly alter surface charge of the NCs, but also leads to steric hindrance. The latter largely decreases the OA growth rate since it increases the energy barrier ( $E_a$ ) of the OA growth.<sup>75</sup>

## **2.4 OA growth controlled by directional-specific interactions: experimental observations**

### 2.4.1 Direct evidence based on *in-situ* HR-TEM experiments

The rapidly-developed *in-situ* high-resolution transmission electron microscopy (HR-TEM) techniques allow for the direct observation of the crystal growth process at the atomic and lattice scales. For instance, Li *et al.* observed the dynamic aligning and attaching process of two iron oxyhydroxide NPs in a fluid cell by *in-situ* HR-TEM and they provided the direct evidence that the OA growth of crystals is governed by strong direction-specific interactions.<sup>87</sup> A typical dynamic attachment process is shown in Figure 12. Figure 12A-G shows that the particles undergo continuous rotation and interaction, and repeatedly touch each other until the attachment is completed when they share the same crystallographic orientation or their orientations are twin-related, as shown in Figure 12H. Careful analysis of the motion behavior reveals that vdW interaction between two NPs provides preliminary attraction to make the assembly of the two NPs. The two NPs remain separated by nanoscale

distances until a proper lattice configuration is established under the decreased energetic barrier due to the change in the Coulombic interaction. To illustrate CI more specifically, the electrostatic repulsion arises from surface cation-cation and anion-anion interactions as the lattices are mismatched, whereas the electrostatic attraction arises from cation-anion interactions in the ionic crystal.

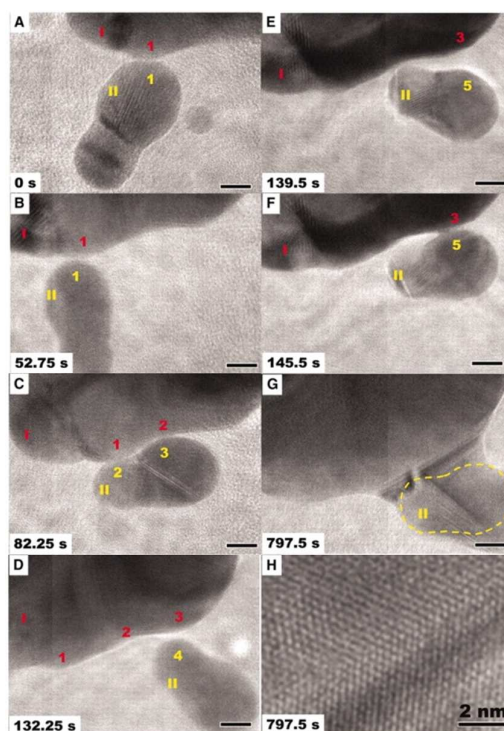


**Figure 12.** (A to G) Typical dynamic *in-situ* HR-TEM images of the attachment process between two particles. The surfaces of particles I and II made transient contact at many points and orientations (points 1-1, 1-2, 2-3, and 3-4) before finally attaching and growing together (points 3-5). (H) High-resolution image of interface in (G) showing twin structure (an inclined twin plane). The yellow dashed line in (G) shows the original boundary of the attached particle. From ref. [87]. Reprinted with permission from AAAS.

Liao *et al.* demonstrated the existence of the electrostatic dipole moments and their dominant role in the shape-directed NP attachment.<sup>88</sup> By tracking the trajectories of Pt<sub>3</sub>Fe NPs in the growth of NRs with the real-time TEM imaging technique, as shown in Figure 13A, the velocity of a spherical NP can be measured as it approaches another spherical NP or a NP chain (Figure 13B). The corresponding forces

associated with these velocities were then calculated and shown in Figure 13B. It indicates that NP movements are random when the NP is above a critical distance from the receiving NP or NP chain. When the NP approaches a spherical NP or a NP chain smaller than a critical distance, the NP experiences a drift velocity, which increases with decreasing distance. The drift velocity increases abruptly at very close distances, indicating the strong attractive forces in short distances. Combining with the preferred attachment of a NP to the two ends of NP chains, they ascribed these phenomena to the anisotropic electrostatic dipolar interactions, which can be generated by particle faceting or surfactants on the NP surface to facilitate the formation of certain patterns. DI between NPs or NP chains is then calculated, which is shown in Figure 13C. Compared with NP-NP interaction, the NP-NP chain interaction is strongly anisotropic, favoring the attachment at the end of the NP chain over the attachment in the middle of the NP chain. The observations and the calculations confirm the dominance of the electrostatic dipolar interactions.

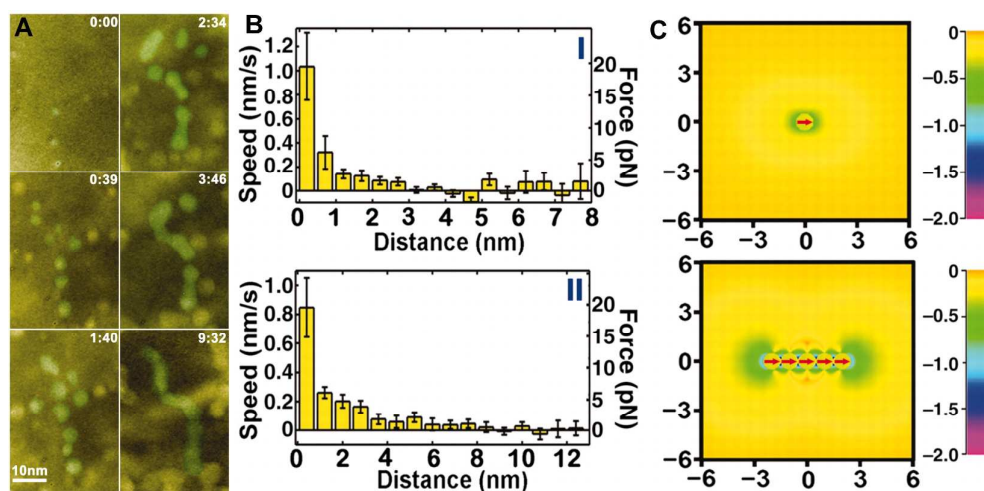


**Figure 13.** (A) Sequential color TEM images of the growth of Pt<sub>3</sub>Fe nanowires in a liquid cell during exposure to the electron beam, showing the evolution from the initial nucleation and growth in the molecular precursor solution to a later stage of nanowire formation by shape-directed NP attachment. Time is displayed as minutes:

seconds. (B) Velocity of a NP when it approaches (I) another NP or (II) a NP chain versus inter-particle distance. Error bars show the standard deviation. The right-hand axis shows forces exerted on the approaching NP. (C) Contour maps of the minimum electrostatic interaction energy exerted by a NP or a NP chain as a NP is approaching (a unit of  $E/k_B T$  has been used, where  $k_B$  is Boltzmann's constant). Each NP is assumed to be a point electronic dipole. It illustrates that the observation of NPs preferring to attach to the ends of a chain is consistent with dipolar forces mediating NP attachment. From ref. [88]. Reprinted with permission from *AAAS*.

With the *in-situ* liquid TEM, Liu *et al.* observed the self-assembly of Au NPs with positively charged cetyltrimethylammonium ions (CTA<sup>+</sup>).<sup>89</sup> Figure 14 shows the time sequential *in-situ* TEM images of the self-assembly process. Under the electron illumination in TEM, the hydrated electrons reduce the overall positive charges of the CTA<sup>+</sup> covered Au NPs, which decreases the repulsive electrostatic forces in the NPs. The anisotropic attractive interactions, including DI and vdW interaction, overcome the repulsion among the NPs and induce the assembly of NPs in the 1D chain. However, the negatively charged Au NPs do not undergo any assembly process and thus still keep separated. The above observation provided the direct evidence that the surface charge induced CI, the anisotropic DI and the vdW interactions govern the kinetics of the OA self-assembly of the NPs. The state of adsorption and the surface charge of NPs indeed largely act on the attachment of NPs and the associated secondary units.

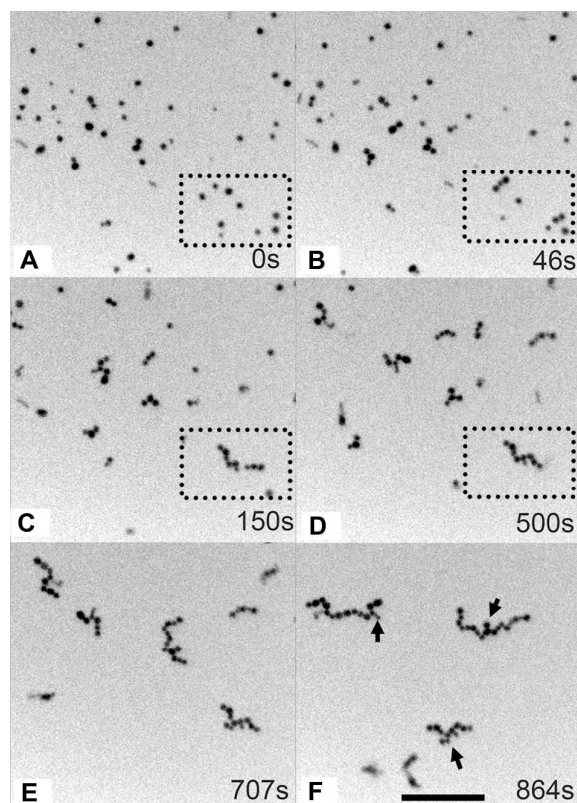


**Figure 14.** The time sequential *in-situ* TEM images of the self-assembly of Au-CTA<sup>+</sup> NPs. (A) At the beginning, NPs are well separated; (B) after 150 s illumination by e-beam with intensity of 10 pA/cm<sup>2</sup>, the dimers, trimers formed; (C and D) the short chains formed by existing dimer, trimer attachment and individual NPs attachment. The scale bar is 500 nm. Reproduced with permission from ref. [89]. Copyright (2013), *American Chemical Society*.

Monitoring NP movements using *in-situ* HR-TEM can provide insightful evidences for strong interactions among NPs. However, such *in-situ* TEM observations must be treated with special caution since the electron beam used in TEM measurements can influence the OA growth. The effects of high-energy electron beam include local heating, direct momentum transfer from the electron beam, and electron charging, which have influence on NC motion and the energies among NCs (vdW, CI, and DI).<sup>90, 91</sup> Thus, any *in-situ* TEM observations should be validated also by *ex-situ* experiments. Nevertheless, *in-situ* HR-TEM technique combined with theoretical methods (MD, MC simulations and DFT calculation) is a powerful method of

exploring the effects of variables influencing the OA growth. These variables include the chemical environments (solvent, ionicity, ligands and other additives), the reaction conditions (temperature, pressure, irradiation, and sonication, etc.) and the crystal structures (lattice structures, crystalline facets and defects).

#### 2.4.2 Roles of DI

DI is the electrostatic interaction between dipoles in NPs. The dipole moments can be classified in two types according to their origin, which are permanent dipoles (PDs) and fluctuating dipoles (FDs). PDs are intrinsic and are induced by crystal structures, polar NP surfaces and surface charges arisen from ligands on NPs. For instance, a CdSe NR has a PD arising from its noncentrosymmetric crystallographic lattice and the PD scales linearly with volume.<sup>92</sup> ZnO nanoplates have intrinsic dipoles along *c*-axis arising from Zn<sup>2+</sup> terminated (0001) planes and O<sup>2-</sup> terminated (000 $\bar{1}$ ) faces.<sup>93</sup> On the other hand, FDs are induced by thermal displacements of individual atoms or ions which vary with time in magnitude and direction. FDs are typically in a much smaller magnitude than PDs and have no permanent direction with respect to nanocrystal orientation.

It is still in debate whether only the permanent dipole interaction (PDI) accounts for the OA growth since the fluctuating dipole interaction (FDI) could also be involved in the OA process. Another debate is about the significance of DI (both PDI and FDI) in the OA growth. A few publications based on both experiments and MD simulations show that DI might be non-prominent in NP-NP interactions at the initial stage of OA

growth.<sup>83,94</sup>

We next take the OA growth of a 1D NR as an example to elucidate the roles of DI in OA growth. The OA growth of NCs has been verified by the above observations to experience multi-step growth processes. In addition, the multi-step growth processes not only occur between two monomer precursors but also occur between secondary particles. Therefore, we can divide the growth of the 1D NR into three sequential stages: fusion of two NPs (NP-NP growth) at the initial stage, oriented attachment of more NPs onto the two end sides of the NR (NR-NP growth), and finally the possible fusion between NRs (NR-NR growth).

If we assume that an OA reaction only involves primary NP monomers (NP-NP growth), its kinetic model can be described by Eq.6,<sup>95</sup>

$$d_t = \frac{d_0(\sqrt[3]{2kt+1})}{kt+1} \quad (6)$$

where  $d_0$  is the diameter of precursor NCs,  $d_t$  is the diameter of NCs at time  $t$ , and  $k$  is the reaction constant. Since OA is typically a thermodynamically metastable state lying between the nucleation stage and OR growth stage, the OR process cannot be ignored and should be distinguished from the OA mechanism. The classic OR kinetics has been well established and can be described by Eq. 7,<sup>96</sup>

$$d_t = \sqrt[3]{d_0^3 + kt} \quad (7)$$

EuS clusters were synthesized through the OA mechanism by thermally annealing 2.5 nm EuS NCs ( $d_0=2.5$  nm) ligated with oleate.<sup>25</sup> As shown in the TEM images of Figure 15, oleate ligands strongly attached to the surface of the EuS NCs below 310 °C. These EuS NCs can only selectively attach to each other at (200) facets,

which results in a relatively low ligand concentration and then the formation of dumbbell structures (Figure 15B) and chains (Figure 15C). The OA growth mechanism governs the reaction at relatively low reaction temperatures. At higher temperatures, the increased thermal momentum of the NCs causes the ligands on EuS NCs to change from oleate to oleylamine, as confirmed by the FT-IR results. Larger aggregations are then formed, as shown in Figure 15D.  $d_t$  is equal to 3.1 nm as the growth time is 180 min. By analyzing the growth kinetics using Eq. 6 and Eq. 7, it is found that OA governs the growth process since the monotonous increase in  $d_t$  predicted according to Eq. 7 is not observed in the experiment. This result verifies that the growth is mainly NP-NP OA growth. Figure 15E shows the characteristic TEM image of the system at 340 °C, which exhibits some NRs in the NC aggregations. The diameters of both the NRs and the NCs are approximately 7.5 nm at  $t = 180$  min. Further kinetic analysis via Eq. 6 and Eq. 7 shows that both the OR mechanism and the single step OA model (Eq. 6) cannot explain the experiment result. A two-step OA reaction mechanism was then found to work well, indicating that a multi-level OA mechanism dominates the reaction at high temperatures. In other words, NR-NP growth must happen. EuS NRs with an aspect ratio  $\sim 15$  were synthesized. Such a long NR growth must have a very high activation energy due to the decreased surface energy. The DI increases with the NR length in the later stage of NR-NP growth, and induces increased attraction forces among particles. This might account for the formation of long NRs. It was recently found by Hapiuk *et al.* that a high external electrical field has negligible influence on the OA growth of bare ZnO NCs.<sup>94</sup>

However, since the NPs both in the experiment of Hapiuk *et al.* and in the MD simulations<sup>83,86</sup> have no ligands or other adsorbed species, the significance of DI in NP-NP growth remains elusive, especially in those occurring in a chemical environments with polar solvent, ions and ligands.

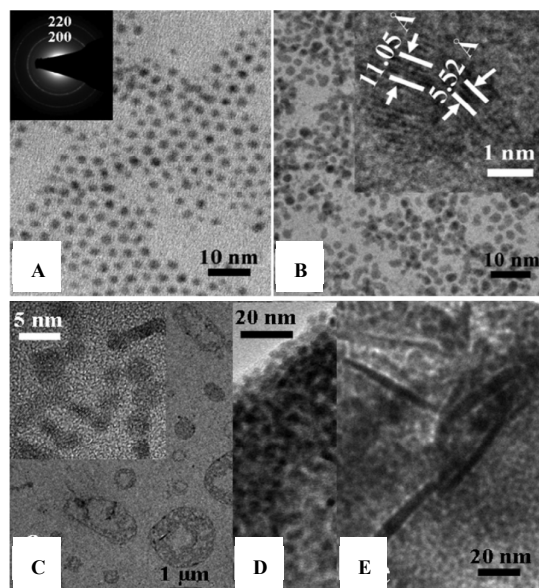


**Figure 15.** (A) TEM image and electron diffraction pattern of 2.5 nm EuS NP monomers, and TEM images of EuS NCs synthesized at (B) 300 °C, (C) 310 °C, (D) 320 °C and (E) 340 °C. The inset of (C) illustrates the chainlike structures that formed and eventually rearranged into clusters. Reprinted with permission from [25]. Copyright (2011), *AIP Publishing LLC*.

In the OA NR-NP growth, which may be a dominant growth type in the growth of OA NRs, the significance of DI is evidenced by the *in-situ* HR-TEM observations shown in Figure 13. The work conducted by Kim *et al.* further confirms the above discussion.<sup>53</sup> They synthesized PbSe NRs by the solution–liquid–solid (SLS) growth of PbSe NPs followed by the OA growth of adjacent PbSe NPs. The morphology of PbSe NRs is shown in the SEM image of Figure 16A and the TEM image of Figure 16B. The HR-TEM image in Figure 16C exhibits the fringe image and corresponding FFT patterns of PbSe NRs, which confirms that the PbSe NRs exhibit high

crystallinity and consist of different lattice orientations (regions (a), (b), (c) correspond to (111), (200) and a mix of (200) and (111) respectively) along the (100) axis. The waved morphology provides the evidence for the OA growth of NRs. The growth mechanism was then proposed by Kim *et al.* as shown in Figure 17. PbSe NPs initially nucleate and grow along the  $\langle 001 \rangle$  direction after the super-saturation is reached with the catalyst of Bi NPs and the selective adsorption of surfactants on the other facets (Figure 17A-B). Through the elongation, the PbSe NPs have the net dipole moments in the  $\langle 001 \rangle$  direction and induces the subsequent attachment of the nearby PbSe NPs (Figure 17C-D). Such dipole moments induce additional dipole moments in the adjacent PbSe NPs such that the OA growth continues until a long NR is formed (Figure 17C-D).

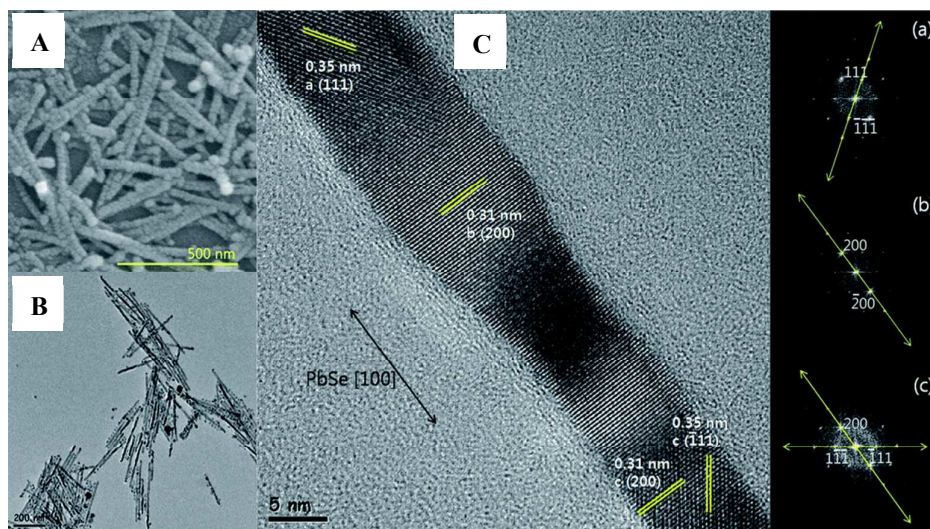


**Figure 16.** High resolution (A) SEM and (B) TEM images of PbSe NRs synthesized using the Bi catalysts. (C) A highly magnified HR-TEM image showing (a) (111) planes, (b) (200) planes and (c) the mixture of (200) and (111) planes, respectively. The insets show the corresponding FFT patterns of (a), (b), and (c), respectively. Reproduced from ref. [53] with permission from *The Royal Society of Chemistry*.

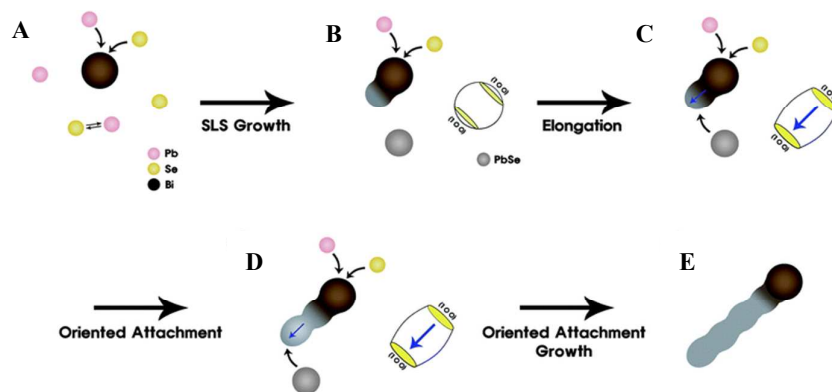


**Figure 17.** Schematic diagram presenting a suggested mechanism for the Bi catalyst induced oriented attachment growth of PbSe NRs. (A) Penetration of Pb and Se elements into Bi catalysts and independent binding between Pb and Se elements. (B) Supersaturation and growth. (C and D) Losing cubic symmetry (dipole moment formation) and subsequent attachment of PbSe NPs, respectively. (E) Final wave-shaped PbSe NRs. Reproduced from ref. [53] with permission from *the Royal Society of Chemistry*.

In the NR-NR growth of OA, DI is crucial in the attachment of two NRs for forming a longer NR. For instance, Gunning *et al.* studied the kinetics of the 1D attachment of CdS NRs with NR lengths of integer times of the original NR length, which eliminated the interference of OR growth.<sup>10</sup> A multi-step kinetic model was employed to study the attachment between two NRs as shown in Figure 18A. Further, a multi-step population balance model was employed as described in Eq. 8,<sup>97</sup>

$$\frac{dN_k}{dt} = \frac{1}{2} \sum_{i+j=k} K_{ij} N_i N_j - N_k \sum_j K_{ij} N_j \quad (8)$$

where  $N_k$  is the concentration of  $A_k$  ( $k$ -mers),  $K_{ij}$  is the rate constants for the reaction between of  $A_i$  and  $A_j$ . The TEM results show that no NRs are longer than the length of a tetramer ( $N_k = 0$  when  $k > 4$ ), and thus no attachment occurs between two dimers ( $K_{22} = 0$ ). Then we have Eq. 9.

$$\frac{d}{dt} \begin{pmatrix} N_1 \\ N_2 \\ N_3 \\ N_4 \end{pmatrix} = \begin{pmatrix} -2K_{11}N_1^2 - K_{12}N_1N_2 - K_{13}N_1N_3 \\ K_{11}N_1^2 - K_{12}N_1N_2 \\ K_{12}N_1N_2 - K_{13}N_1N_3 \\ K_{13}N_1N_3 \end{pmatrix} \quad (9)$$

These equations are too complex to be solved analytically, but can be solved numerically by the dataset fitting of the concentration time differentials using the concentrations as independent variables. With  $N_k$  set as integers, the values of  $K_{lj}$  ( $1 \leq j \leq 3$ ) at different temperatures were obtained by fitting the experimental data. The activation energy and Arrhenius frequency factor are then solved from the Arrhenius plots. The plots of  $E_a$  and  $\ln A$  versus rod AR are shown in Figure 18B. Gunning *et al.* further explained why the OA growth of too short a NR or too long a NR cannot occur (as shown in the shadow area in Figure 18B) by analyzing the factors at the two stages of the OA growth: alignment and fusion. The alignment stage is dominated by the frequency factor, which was assumed in the study to be dependent on the dipole moment. The electrical dipole interaction ( $E_{DI}$ ) was estimated to be proportional to the average length of the NR ( $\bar{l}$ ) as shown in Eq. 10.

$$E_{DI} \propto \bar{l} \quad (10)$$

This equation demonstrates that the  $E_{DI}$  associated with NRs is the driving force for the ordered 1D alignment of NRs. The electrical dipole interaction determines the Arrhenius frequency factor and is dependent on the NR length for a given material.  $E_{DI}$  and  $A$  increase as the length of NR increases as confirmed by the blue curve shown in Figure 18B. When the NRs are too short, no attachment occurs owing to ineffective alignment, which is marked by the lower hatched area in Figure 18B. For too long a NR, the fusion surface energy is decreased, which then leads to the sharp

increase in the activation energy of the OA growth (the orange curve in Figure 18B) as well as the decreased upper limit of the NR elongation. The 1D OA systems between two NRs with a reduced dimensionality, simple metrology and limited extent of the NR elongation are efficient prototypes to analyze the early stages of an OA growth. Although this model is based on a special NR-NR attachment and cannot be directly applied to general situations such as the oriented attachment between two NPs and between a NP and a NR, it indeed verifies the importance of DI to the OA NC growth. There is little literature about the OA growth via NR-NR. There may be an alternative way other than NR-NP to grow NRs with ultra-high aspect ratios.

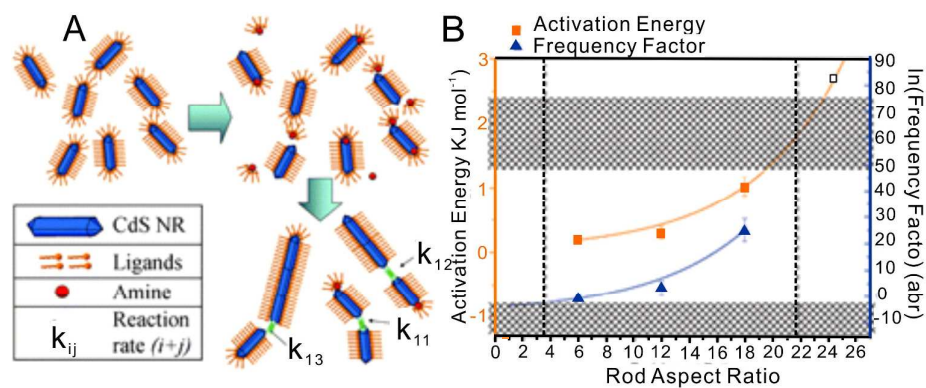


**Figure 18.** (A) A schematic representation of the oriented attachment between two NRs. (B) A plot of  $E_a$  and  $\ln A$  versus rod aspect ratio. The upper hatched area represents the energies that are too high for rod fusion to occur and the lower hatched area represents the frequencies that are too few to allow adequate alignment for fusion to occur. Reproduced from ref. [10] with permission from *the PCCP Owner Societies*.

The dipole-induced electrostatic interaction can drive the OA process and the self-assembly even in more complex 2D or 3D mesocrystals besides 1D NRs. Liu *et al.* synthesized the nanobelt-based, core-shell ZnO apple-like microspheres as shown in Figure 19A-B.<sup>98</sup> The ZnO microsphere assembly is formed from 2D nanoplatelets, driven by the intrinsic dipole field arising from the anisotropic adsorption of surfactants on the (0001) facet of the ZnO crystal. The dipole-directed growth model

is shown in Figure 19C. First, the hexagonal nanoplatelets are formed under the selective adsorption of the negatively charged polymer which contains  $\text{Zn}^{2+}$  terminated (0001) faces and  $\text{O}^{2-}$  terminated (000 $\bar{1}$ ) faces, as well as intrinsic dipole moments along the  $c$ -axis. The 3D stacking of the twin structures can occur with the positively charged (0001) plane as the attachment facet while the negatively-charged polymer can act as a matrix between the two attaching facets. When adding all the microscopic dipoles, a unique twinned macroscopic electrical dipole system is formed, resulting in the growth of the apple-like structures through the attraction of the negatively-charged polymer-stabilized intermediates and dipolar nanoplatelets in three dimensions. The assembly of the nanoplatelets into a parallel outer shell structure is also induced by the synergistic effects of the core and the dipolar outer shell nanoplatelets. The simulation results of the electrostatic potential distributions of the twinned core structure in Figure 19D, the synergistic generated electric field, the electrostatic potential in the core, and the dipoles of the nanoplatelets in the shell, as shown in Figure 19E, further confirm that the dipole-field-driven mechanism induces the formation of the apple-like structures. This example suggests that upon controlling DI between the attaching NPs, OA might be employed to synthesize various 3D nanostructures.

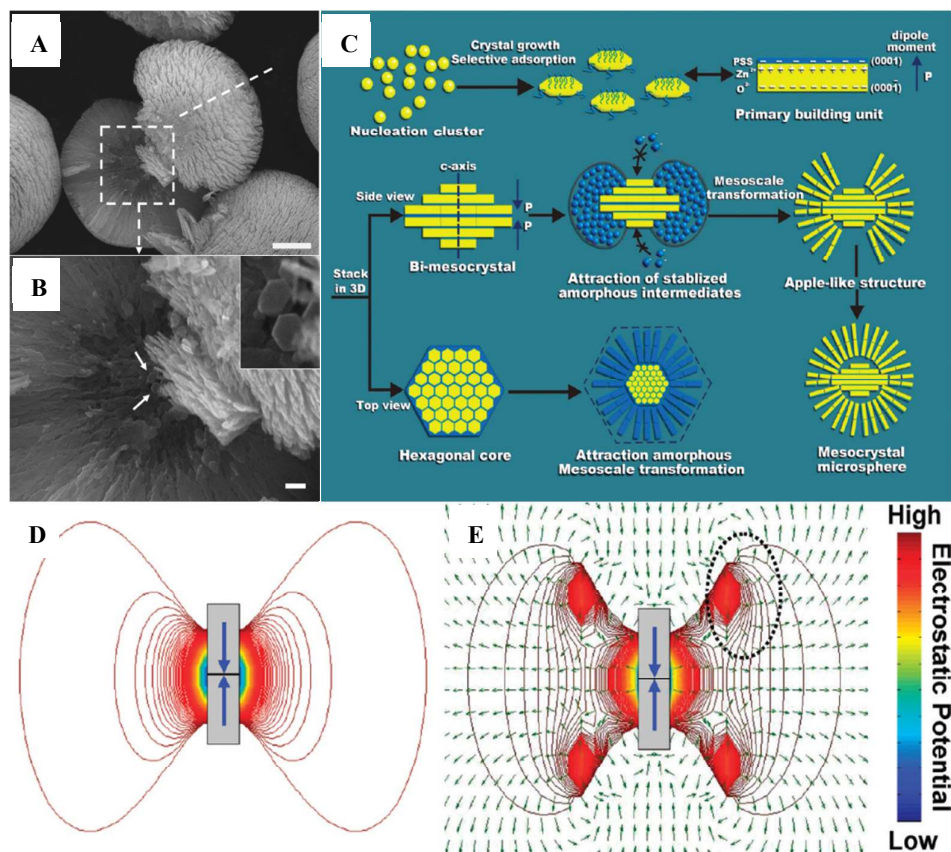


**Figure 19.** (A) SEM image of a cracked ZnO microsphere. The dashed line is the axis of the microsphere. (B) The detailed inner structure of the cracked ZnO microsphere. The arrows point to the distinct individual nanoplalelets on the surface. The inset is the magnified figure of the area that the arrows point to. Scale bar: (A) 1  $\mu\text{m}$  and (B) 200 nm. (C) Schematic illustration of the growth model. (D) Contour plot of the electrostatic potential distribution (color lines) around the model prism. The model prism (the gray rectangle) consists of permanent dipoles (the blue arrows). (E) The electric field (green arrows which also represent the dipoles) and electrostatic potential distributions of the model prism, which takes the dipoles of the nanoplalelets on the shell into consideration. The green arrows indicate how the nanoplalelets are surrounding the core, because the spatial orientation of a nanoplalelet is normal to its dipole. The electric field distribution near the dipoles, which stand for the intrinsic dipoles of nanoplalelets near the hole, is marked by the black dashed circle. The color chart represents the intensity of the electrostatic potential. The distribution is shown in the Y-Z plane. All the data to calculate the electric potential are used as natural units. Reproduced with permission from ref. [98]. Copyright (2009) *American Chemical Society*.

### 3. Summary and outlook

This review summarizes the OA growth kinetics from an energy point of view, with the aim of understanding the underlining energetic interactions in the OA crystal growth and the correlation between the kinetic processes with the resulted

morphologies of OA crystals. The roles of various interactions mainly including vdW, CI and DI to the OA growth kinetics are overviewed. The correlation between the interactions of colloidal spherical NPs with experimental conditions including ionic strength, pH, surface potential, Hamaker coefficient and dielectric constant, is evaluated with a systematic insight into the DLVO theory. It has been found that the DLVO model does not account for primary particles with anisotropic shapes or the dynamic size change in the growth of OA crystals. The development of the dynamic 1D growth model facilitates the evaluation of the OA growth process. Such a model based on the derived analytical expressions of vdW and CI between an attaching NP and a growing NR, allows for the quantitative investigation into the correlation between the growth kinetics of OA NRs and the important parameters associated with the OA growth. The theoretical investigation focuses on the crystal evolution throughout the dynamic growth process, and thus improves our fundamental understanding on the 1D growth OA NCs. The molecular mechanics, molecular dynamics and DFT simulations provide further insight into the OA growth at crystalline, molecular and even atomic levels. Such information reveals the origin of the force field between NPs, the collision mode, the bonding, the preferred attachment orientations and the resulted morphology of the OA crystal. All of the factors have barely been observed experimentally. But more accurate OA growth models for large numbers of nanoscale components remain unexplored. The advances in the experimental techniques facilitate the direct *in-situ* observations of the OA assembly, and allow one to track the trajectory of attaching NCs. The force field between NPs

can be extracted from the movement and attachment of NCs. These results provide first-hand evidences of the interactions between NPs and their dominant role in the shape-directed NP attachment. Nevertheless, when the research system is macro-scale, more influencing factors must be considered to study the OA growth kinetics. The evaluation of the nano/meso-scale interactions between various assembling components in experimental conditions demands further insightful studies.

Undoubtedly, the OA crystal growth has developed into a fundamental materials field and the rapid progress in both theories and experiments is expected to occur in the years to come. Further studies of inter-particle interactions in various experimental conditions, such as advanced *in-situ* HR-TEM technique and computer simulation *via* more practical models, will improve our understanding on the OA growth mechanism and enable the rational design of materials with novel structures, properties and application potentials.

## References

1. R. L. Penn and J. F. Banfield, *Science*, 1998, **281**, 969-971.
2. C. J. Dalmaschio, C. Ribeiro and E. R. Leite, *Nanoscale*, 2010, **2**, 2336-2345.
3. N. D. Burrows, V. M. Yuwono and R. L. Penn, *MRS Bull.*, 2010, **35**, 133-137.
4. J. Zhang, F. Huang and Z. Lin, *Nanoscale*, 2010, **2**, 2873-2873.
5. Q. Zhang, S. J. Liu and S. H. Yu, *J. Mater. Chem.*, 2009, **19**, 191-207.
6. T. P. Almeida, M. W. Fay, Y. Q. Zhu, P. D. Brown, *Nanoscale*, **2010**, **2**, 2390-2399.
7. E. J. Choi and Y. D. Huh, *Bull. Korean Chem. Soc.*, 2010, **31**, 196-198.
8. P. D. Christy, N. Melikechi, N. S. N. Jothi, A. R. B. Suganthi and P. Sagayaraj, *J. Nanopart. Res.*, 2010, **12**, 2875-2882.
9. Y. M. Cui, L. Liu, Y. Chen, D. H. Yu, X. F. Zhou, N. P. Xu and W. P. Ding, *Solid State Sci.*, 2010, **12**, 232-237.
10. R. D. Gunning, C. O'Sullivan and K. M. Ryan, *Phys Chem Chem Phys*, 2010, **12**, 12430-12435.
11. Y. H. Kim, J. H. Lee, D. W. Shin, S. M. Park, J. S. Moon, J. G. Nam and B. Yoo, *Chem. Commun.*, 2010, **46**, 2292-2294.
12. W. K. Koh, A. C. Bartnik, F. W. Wise and C. B. Murray, *J. Am. Chem. Soc.*, 2010, **132**, 3909-3913.
13. C.T. Lo and P.Y. Kuo, *J. Phys. Chem. C*, 2010, **114**, 4808-4815.
14. J. J. Ning, K. K. Men, G. J. Xiao, B. Zou, L. Wang, Q. Q. Dai, B. B. Liu and G. T. Zou, *Crystengcomm*, 2010, **12**, 4275-4279.

15. C. Schliehe, B. H. Juarez, M. Pelletier, S. Jander, D. Greshnykh, M. Nagel, A. Meyer, S. Foerster, A. Kornowski, C. Klinke and H. Weller, *Science*, 2010, **329**, 550-553.
16. B. B. Srivastava, S. Jana, D. D. Sarma and N. Pradhan, *J. Phys. Chem. Lett.*, 2010, **1**, 1932-1935.
17. J. S. Zheng, F. Huang, S. G. Yin, Y. J. Wang, Z. Lin, X. L. Wu and Y. B. Zhao, *J. Am. Chem. Soc.*, 2010, **132**, 9528-9530.
18. J. Y. Chang, M. H. Tsai, K. L. Ou, C. H. Yang and J. C. Fan, *Crystengcomm*, 2011, **13**, 4236-4243.
19. J. S. Chen, T. Zhu, C. M. Li and X. W. Lou, *Angew. Chem., Int. Ed. Engl.*, 2011, **50**, 650-653.
20. R. O. Da Silva, R. H. Goncalves, D. G. Stroppa, A. J. Ramirez and E. R. Leite, *Nanoscale*, 2011, **3**, 1910-1916.
21. F. Dong, W. K. Ho, S. C. Lee, Z. B. Wu, M. Fu, S. C. Zou and Y. Huang, *J. Mater. Chem.*, 2011, **21**, 12428-12436.
22. F. Dong, S. C. Lee, Z. B. Wu, Y. Huang, M. Fu, W. K. Ho, S. C. Zou and B. Wang, *J. Hazard Mater.*, 2011, **195**, 346-354.
23. X. C. Duan, X. D. Liu, Q. Chen, H. B. Li, J. Li, X. Hu, Y. Y. Li, J. M. Ma and W. J. Zheng, *Dalton Trans.*, 2011, **40**, 1924-1928.
24. L. F. Fei, J. K. Yuan, Y. M. Hu, C. Z. Wu, J. L. Wang and Y. Wang, *Cryst. Growth. Des.*, 2011, **11**, 1049-1053.
25. W. He and J. H. Dickerson, *Appl. Phys. Lett.*, 2011, **98**, 081914.
26. N. Huang, C. Sun, M. W. Zhu, B. Zhang, J. Gong and X. Jiang, *Nanotechnology*, 2011, **22**, 265612.
27. R. C. Jin, G. Chen, Q. Wang and J. A. Pei, *Mater. Lett.*, 2011, **65**, 1151-1153.
28. D. Koziej, M. D. Rossell, B. Ludi, A. Hintennach, P. Novak, J. D. Grunwaldt and M. Niederberger, *Small*, 2011, **7**, 377-387.
29. K. R. Krishnadas, P. R. Sajanlal and T. Pradeep, *J. Phys. Chem. C*, 2011, **115**, 4483-4490.
30. M. Li, F. Y. Kong, H. Q. Wang and G. H. Li, *Crystengcomm*, 2011, **13**, 5317-5320.
31. Z. Li, J. Sui, X. Li and W. Cai, *Langmuir*, 2011, **27**, 2258-2264.
32. L. X. Lin, Z. H. Li, Y. Zheng and A. S. Ahmed, *Nanotechnology*, 2011, **22**, 215603.
33. Y. X. Liu, D. S. Wang, Q. Peng, D. R. Chu, X. W. Liu and Y. D. Li, *Inorg. Chem.*, 2011, **50**, 5841-5847.
34. M. L. Moreira, J. Andres, V. R. Mastelaro, J. A. Varela and E. Longo, *Crystengcomm*, 2011, **13**, 5818-5824.
35. M. A. Sliem, A. Chemseddine, U. Bloeck and R. A. Fischer, *Crystengcomm*, 2011, **13**, 483-488.
36. D. G. Stroppa, L. A. Montoro, A. Beltran, T. G. Conti, R. O. da Silva, J. Andres, E. R. Leite and A. J. Ramirez, *Chem. Commun.*, 2011, **47**, 3117-3119.
37. T. Taniguchi, K. Katsumata, S. Omata, K. Okada and N. Matsushita, *Cryst. Growth. Des.*, 2011, **11**, 3754-3760.
38. Y. Tian, J. Tian, X. Li, B. B. Yu and T. Shi, *Chem. Commun.*, 2011, **47**, 2847-2849.
39. D. D. Vaughn, S. I. In and R. E. Schaak, *ACS Nano*, 2011, **5**, 8852-8860.
40. K. Wang, H. W. Liang, W. T. Yao and S. H. Yu, *J. Mater. Chem.*, 2011, **21**, 15057-15062.
41. Y. Tian, H. Y. Yang, K. Li and X. Jin, *J. Mater. Chem.*, 2012, **22**, 22510-22516.
42. Q. Wang, G. Chen, X. R. Shi, R. C. Jin, L. Wang and D. H. Chen, *Powder Technol.*, 2011, **207**, 192-198.
43. Q. Y. Wang, X. C. Yang, J. W. Hou, M. Huang and Y. H. Zhao, *Appl. Surf. Sci.*, 2011, **257**, 5857-5862.
44. A. Yella, U. K. Gautam, E. Mugnaioli, M. Panthofer, Y. Bando, D. Golberg, U. Kolb and W. Tremel, *Crystengcomm*, 2011, **13**, 4074-4081.
45. Y. K. Yin, F. H. Yang, Y. Yang, Z. B. Gan, Z. M. Qin, S. Gao, B. B. Zhou and X. X. Li, *Superlattice Microst.*, 2011, **49**, 599-607.
46. H. Zhang, J. Huang, X. G. Zhou and X. H. Zhong, *Inorg. Chem.*, 2011, **50**, 7729-7734.
47. N. D. Burrows, C. R. H. Hale and R. L. Penn, *Cryst Growth Des.*, 2012, **12**, 4787-4797.
48. X. Y. Chen, Y. Zhou, Q. Liu, Z. D. Li, J. G. Liu and Z. G. Zou, *ACS Appl. Mater. Inter.*, 2012, **4**, 3372-3377.
49. M. Distaso, M. Mackovic, E. Spiecker and W. Peukert, *Chem.-Eur. J.*, 2012, **18**, 13265-13268.
50. F. Dong, Y. J. Sun, M. Fu, Z. B. Wu and S. C. Lee, *J. Hazard Mater.*, 2012, **219**, 26-34.
51. F. J. Douglas, D. A. MacLaren, C. Renero-Lecuna, R. D. Peacock, R. Valiente and M. Murrie, *Crystengcomm.*, 2012, **14**, 7110-7114.

52. Z. H. Ji, D. Dong, H. L. Guo, Y. M. Chai, Y. P. Li, Y. Q. Liu and C. G. Liu, *Mater. Chem. Phys.*, 2012, **136**, 831-836.
53. M. S. Kim and Y. M. Sung, *Crystengcomm*, 2012, **14**, 1948-1953.
54. Z. Q. Li, X. S. Lin, L. Zhang, X. T. Chen and Z. L. Xue, *Crystengcomm*, 2012, **14**, 3495-3500.
55. H. Y. Liang, H. G. Zhao, D. Rossouw, W. Z. Wang, H. X. Xu, G. A. Botton and D. L. Ma, *Chem.Mater.*, 2012, **24**, 2339-2346.
56. M. H. Liu, Y. H. Tseng, H. F. Greer, W. Z. Zhou and C. Y. Mou, *Chem.-Eur. J.*, 2012, **18**, 16104-16113.
57. Z. Liu, H. Zhou, Y. S. Lim, J. H. Song, L. Piao and S. H. Kim, *Langmuir*, 2012, **28**, 9244-9249.
58. B. Ludi, M. J. Suess, I. A. Werner and M. Niederberger, *Nanoscale*, 2012, **4**, 1982-1995.
59. C. Wang, G. H. Du, K. Stahl, H. X. Huang, Y. J. Zhong and J. Z. Jiang, *J. Phys. Chem. C.*, 2012, **116**, 4000-4011.
60. H. Wang, Y. Liu, Z. Liu, H. M. Xu, Y. J. Deng and H. Shen, *Crystengcomm*, 2012, **14**, 2278-2282.
61. Y. L. Cao, P. F. Hu and D. Z. Jia, *Applied Surface Science*, 2013, **265**, 771-777.
62. Z. K. Cui, L. W. Mi and D. W. Zeng, *J. Alloy Compd.*, 2013, **549**, 70-76.
63. B. J. Li, X. M. Xu, Y. B. Zhao and Z. J. Zhang, *Mater. Res. Bull.*, 2013, **48**, 1281-1287.
64. D. S. Li, F. Soberanis, J. Fu, W. T. Hou, J. Z. Wu and D. Kisailus, *Cryst. Growth Des.*, 2013, **13**, 422-428.
65. F. Li, J. Xu, L. Chen, B. B. Ni, X. N. Li, Z. P. Fu and Y. L. Lu, *J. Mater. Chem. A*, 2013, **1**, 225-228.
66. J. Li, X. H. Liu, Q. F. Han, X. X. Yao and X. Wang, *J. Mater. Chem. A*, 2013, **1**, 1246-1253.
67. R. Liu, F. L. Liu, S. Q. Zhao, Y. L. Su, D. J. Wang and Q. Shen, *Crystengcomm*, 2013, **15**, 509-515.
68. S. Nootchanat, C. Thammacharoen, B. Lohwongwatana and S. Ekgasit, *Rsc Advances*, 2013, **3**, 3707-3716.
69. M. Shuai, A. F. Mejia, Y. W. Chang and Z. D. Cheng, *Crystengcomm*, 2013, **15**, 1970-1977.
70. H. Song, K. H. Lee, H. Jeong, S. H. Um, G. S. Han, H. S. Jung and G. Y. Jung, *Nanoscale*, 2013, **5**, 1188-1194.
71. X. F. Yu, D. S. Wang, Q. Peng and Y. D. Li, *Chem.Eur. J.*, 2013, **19**, 233-239.
72. M. Elimelech, X. Jia, J. Gregory and R. Williams, *Particle deposition & aggregation: measurement, modelling and simulation*, Butterworth-Heinemann, 1998.
73. K. J. Bishop, C. E. Wilmer, S. Soh and B. A. Grzybowski, *small*, 2009, **5**, 1600-1630.
74. A. R. Petosa, D. P. Jaisi, I. R. Quevedo, M. Elimelech and N. Tufenkji, *Environ. Sci. Technol.*, 2010, **44**, 6532-6549.
75. D. Grasso, K. Subramaniam, M. Butkus, K. Strevett and J. Bergendahl, *Rev. Environ. Sci. Biotechnol.*, 2002, **1**, 17-38.
76. N. Ise and I. Sogami, *Structure Formation in Solution: Ionic Polymers and Colloidal Particles Edited by N. Ise and I. Sogami. Berlin: Springer*, 2005.
77. W. D. He, J. H. Lin, X. Lin, N. Lu, M. Zhou, K. H. L. Zhang, *Analyst*, 2012, **137**, 4917-4920.
78. W. D. He, J. H. Lin, B. Wang, S. Q. Tuo, S. T. Pantelides and J. H. Dickerson, *Phys. Chem. Chem. Phys.*, 2012, **14**, 4548-4553.
79. W.D. He, *CrystEngComm* 2013, in press. DOI: 10.1039/C3CE4064F.
80. W. D. He, Y. Q. Zhang, J. H. Dickerson, X. Lin, H. L. Lu, K.C.Wen, X. N. Wang, *Analyst*, 2013, in press, DOI: 10.1039/C3AN01261A.
81. Y. H. Kim, J. H. Lee, D. W. Shin, S. M. Park, J. S. Moon, J.G. Nam and J. B. Yoo, *Chem. Comm.*, 2010, **46**, 2292-2294.
82. H. Zhang and J. F. Banfield, *J. Phy. Chem. Lett.*, 2012, **3**, 2882-2886.
83. M. Alimohammadi and K. A. Fichthorn, *Nano lett.*, 2009, **9**, 4198-4203.
84. R. Sathiyarayanan, M. Alimohammadi, Y. Zhou and K. A. Fichthorn, *J. Phy. Chem. C*, 2011, **115**, 18983-18990.
85. M. Giersig, I. Pastoriza-Santos, L.Liz-Marzan, *J. Mater. Chem.*2004, **14**, 607.
86. P. Schapotschnikow, M. A. Van Huis, H. W. Zandbergen, D. Vanmaekelbergh and T. J. Vlugt, *Nano Lett.* 2010, **10**(10): 3966-3971.
87. D. Li, M. H. Nielsen, J. R. Lee, C. Frandsen, J. F. Banfield and J. J. De Yoreo, *Science*, 2012, **336**, 1014-1018.
88. H.G. Liao, L. Cui, S. Whitelam and H. Zheng, *Science*, 2012, **336**, 1011-1014.
89. Y. Liu, X.M. Lin, Y. Sun and T. Rajh, *J. Am. Chem. Soc.*, 2013, **135**(10), 3764-3767.

90. R. F. Egerton and P. Li, M. Malac, *Micron*. 2004, **35**, 399-409.
91. M. Zheng, S. A. Claridge, A. M. Minor, A. P. Alivisatos, and U. Dahmen, *Nano Lett.* 2009, **9**, 2460-2465.
92. L. S. Li, A. P. Alivisatos, *Phys. Rev. Lett.* 2003, **90**, 097402-097405.
93. A. Taubert, D. Palms, Ö. Weiss, M.T. Piccini and D.N. Batchelder, *Chem. Mater*, 2002, **14**(6): 2594-2601.
94. Hapiuk, B. Masenelli, K.Masenelli-Varlot, D.Tainoff, O. Boisron, C. Albin, and P. Melinon, *J. Phys. Chem. C* 2013, **117**, 10220–10227.
95. F. Huang, H. Z. Zhang, and J. F. Banfield, *Nano. Lett.*, 2003, **3**, 373-378.
96. A. J. Ardell, *Acta. Metall. Mater.*, 1972, **20**(4), 601-609.
97. D. Van Hying, W. Klemperer, C. Zukoski, *Langmuir*, 2001, **17**, 3128-3135.
98. Z. Liu, X. Wen, X. Wu, Y. Gao, H. Chen, J. Zhu and P. Chu, *J. Am. Chem. Soc.*, 2009, **131**, 9405-9412.